Editors' Choice - Dealloying-Driven Cerium Precipitation on Intermetallic Particles in Aerospace Aluminium Alloys

Kosari, A.; Ahmadi, M.; Tichelaar, F.; Visser, P.; Gonzalez-Garcia, Y.; Zandbergen, H.; Terryn, H.; Mol, J. M.C.

Important note
To cite this publication, please use the final published version (if applicable).
Please check the document version above.

The Electrochemical Society
Advancing solid state & electrochemical science & technology

Editors' Choice—Dealloying-Driven Cerium Precipitation on Intermetallic Particles in Aerospace Aluminium Alloys

To cite this article: A. Kosari *et al* 2021 *J. Electrochem. Soc.* **168** 041505

View the article online for updates and enhancements.

Editors' Choice—Dealloying-Driven Cerium Precipitation on Intermetallic Particles in Aerospace Aluminium Alloys

A. Kosari,[1] M. Ahmadi,[2] F. Tichelaar,[2] P. Visser,[3] Y. Gonzalez-Garcia,[1] H. Zandbergen,[2] H. Terryn,[4,*] and J. M. C. Mol[1,z]

[1]*Department of Materials Science and Engineering, Delft University of Technology, 2628 CD Delft, The Netherlands*
[2]*Kavli Institute of Nanoscience, Delft University of Technology, 2628 CJ Delft, The Netherlands*
[3]*AkzoNobel, 2171 AJ, Sassenheim, The Netherlands*
[4]*Department of Materials and Chemistry, Research Group Electrochemical and Surface Engineering (SURF), Vrije Universiteit Brussel, 1050 Brussels, Belgium*

Cerium-based compounds have been studied for decades as non-toxic candidates for the protection of aerospace aluminium alloys (AAs) like AA2024-T3. However, the complex heterogeneous microstructure of these alloys has hindered a thorough understanding of the subsequent stages of corrosion protection provided by this class of inhibitors. Thus, this work is devoted to unravelling the interaction mechanisms of different intermetallic particles (IMPs) in AA2024-T3 with cerium nitrate at the nanoscopic scale. This has been fulfilled through detailed top-view and cross-sectional analytical TEM investigations along with electrochemical evaluations. In line with our recent findings, we here report dealloying of IMPs as the main factor governing the rate of local cerium precipitation in contrast to micro-galvanic corrosion between IMPs and the surrounding matrix. Furthermore, we discuss a connection between the electrochemical response of the AA2024-T3 system and the morphological and compositional evolutions of individual IMPs including Al_2CuMg, Al_2Cu, $Al_7Cu_2Fe(Mn)$ and $Al_{76}Cu_6Fe_7Mn_5Si_6$ at different stages of a 96-h exposure.

Aerospace aluminium alloys (AAs) are a class of structural materials that contain intermetallic compounds including precipitates, constituent particles and dispersoids ranging from nano- to micrometre scales. In AA2024-T3, Al_2CuMg and Al_2Cu are precipitates that appear in response to age hardening processes while constituent phases like $Al_7Cu_2Fe(Mn)$ and $Al_{76}Cu_6Fe_7Mn_5Si_6$ are formed during solidification, contributing, to different extents, to the mechanical strength of the alloy.[1] In terms of corrosion, intermetallic particles (IMPs) are electrochemically active locations in the alloy matrix at which local corrosion attack evidently takes place.[2–7] Therefore, the use of inhibitors that can effectively impede the local electrochemical activity of IMPs is necessary to prevent local stress concentrations and eventually the loss of structural integrity of AA applications. For decades, this purpose has reliably been fulfilled via hexavalent-chromium based chemistries, in spite of their undesirable impact on health and the environment.[8–10] However, due to strict international health and safety legislation, they have to be entirely replaced with non-toxic and efficient inhibitive systems in the near future.[11]

Following that, cerium-based compounds have been introduced as promising non-toxic inhibitors and examined extensively to inhibit localized corrosion of AAs.[12–24] The main protective properties of this group of inhibitors are attributed to the formation of insoluble cerium (hydr)oxide precipitate via a chemical route and as a response to the local alkalinity established by the electrochemical activity of individual IMPs (microgalvanic corrosion).[25,26] However, the literature still lacks an agreement when it comes to explaining the detailed mechanisms in relation to the morphology and sequence of cerium (hydr)oxide precipitation on individual intermetallic compounds. For instance, according to Paussa et al.,[27] local alkalisation at magnesium-rich regions of a corroding S-phase (Al_2CuMg) can trigger cerium precipitation. However, Li et al.[28] proposed initial cerium precipitate as a consequence of electrochemical transition of S-phase from an anodic to a cathodic particle (nobility inversion), after which the precipitate continues to thicken. Aldykewicz et al.[29] merely detected cerium on Cu-rich IMPs and not on Fe/Mn-containing IMPs. In contrast, Yasakau et al.[26] found a cerium deposit on a Fe-containing particle, appearing in a nodular morphology. In addition, Campestrini et al. proposed the Cu redeposition as a critical condition to form a thick cerium oxide layer otherwise the IMPs do not function as preferential nucleation sites during the conversion process.[30] Besides, morphological and compositional evolutions of θ-phase (Al_2Cu) during the interaction with cerium-based inhibitors has not been addressed in the literature yet.

Therefore, the current work is devoted to exploring detailed interaction mechanisms of cerium nitrate, as an effective and efficient inhibitor,[31,32] with different types of intermetallic compounds in AA2024-T3. In fact, we put efforts into correlating the conventional electrochemical response and the nanoscopic morphological and compositional evolutions related to different IMPs over an exposure up to 96 h. A challenge in this regard is the complicated electrochemical behaviour of IMPs themselves, including their nanoscopic morphological and compositional evolution with time. Recently, we reported a dealloying-driven local corrosion initiation mechanism for both conventional anodic and cathodic intermetallic phases.[33,34] Besides, we brought up the intrinsic electrochemical instability of intermetallic compounds as a dominant factor controlling the kinetics of local degradation.[33,34] Here, we further address how the dealloying process and electrochemical stability can establish a local solution chemistry driving cerium precipitation over IMPs. To this aim, we initially record open circuit potential (OCP) and linear polarization resistance (LPR) of AA2024-T3 samples exposed to a cerium-containing solution along with general top-view morphological observations of the surface. Furthermore, detailed top-view and cross-sectional analytical transmission electron microscopy (TEM) on individual Al_2CuMg, Al_2Cu, $Al_7Cu_2Fe(Mn)$ and $Al_{76}Cu_6Fe_7Mn_5Si_6$ particles are carried out to provide nanoscopic insights into the inhibition mechanism at different stages of exposure and particularly related to the different intermetallic chemistries.
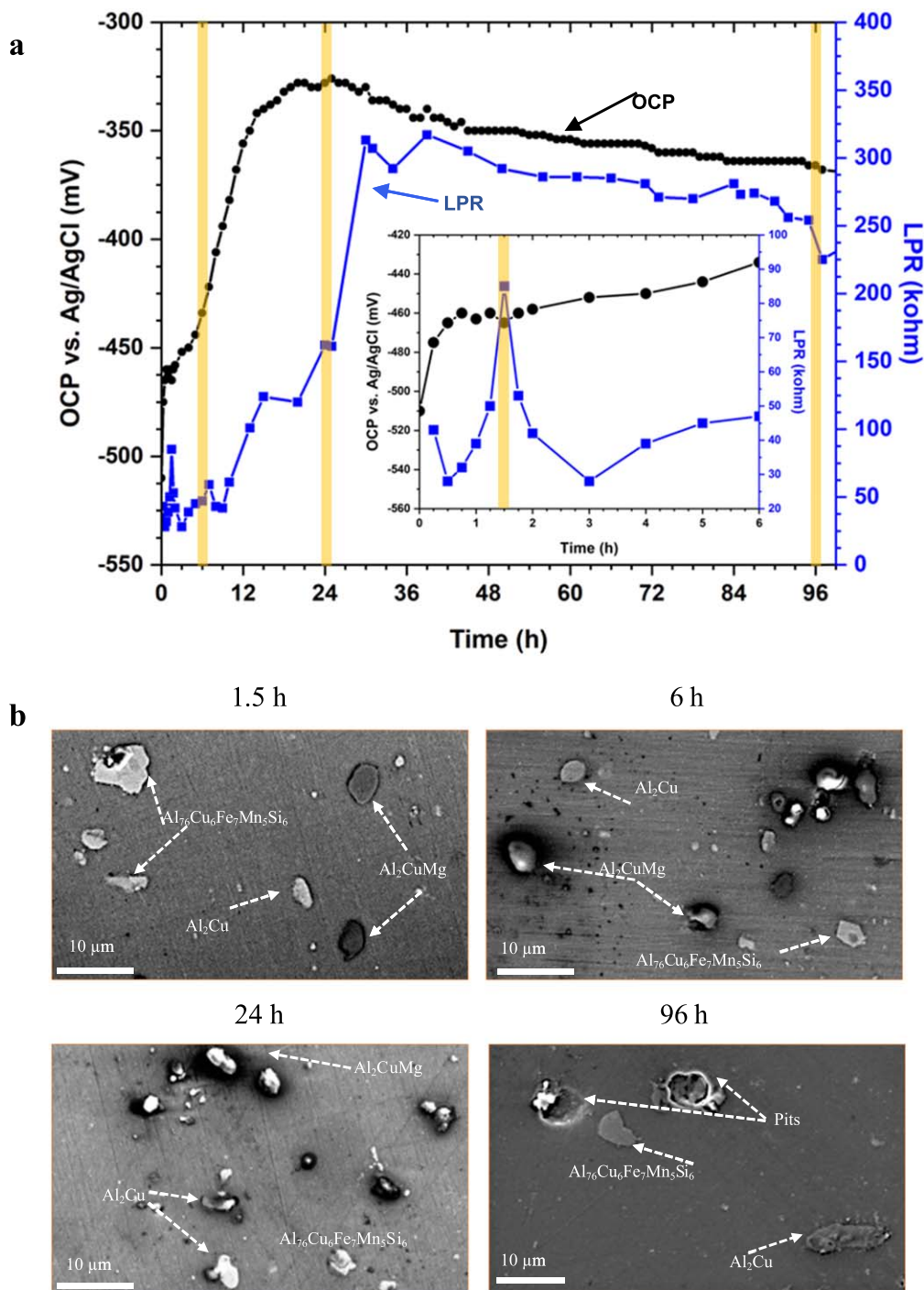
Figure 1. General electrochemical and morphological analysis with time. (a) OCP (Black line with circle markers) and LPR (Blue line with rectangle markers) values recorded for the AA2024-T3 sample continuously exposed to 0.01 M NaCl + 0.003 M Ce(NO₃)₃ solution for 96 h. (b) Top-view SEM images of the exposed samples after different exposure times. The images are acquired by collecting the secondary electrons (SE) at an acceleration voltage of 10 kV.

Experimental

Electrochemical evaluations.—Prior to electrochemical measurements, AA2024-T3 sheets were ground down to #1200 and then polished on a soft cloth in alumina slurries of 0.5 and 0.05 μm, respectively, in a non-aqueous solution. The freshly-polished samples of 3.14 cm^2 were exposed to 0.01 M NaCl + 0.003 M Ce(NO₃)₃ solution (pH = 5.2) for a period of 96 h while the OCP values were monitored continuously vs an Ag/AgCl saturated reference electrode. Besides, the superimposed LPR measurements were carried out every 15 min during the first 2 h and every 1 h for the rest of the

exposure with an amplitude of ±10 mV vs the OCP at a scan rate of 1 mV/s and in a conventional three-electrode set-up. The LPR values were estimated by considering the linear part (i.e., slope) of potential vs current curves around the OCP.

Analytical TEM studies.—Top-view quasi in situ TEM analysis was conducted on argon ion-milled 3-mm disks intermittently exposed to 0.01 M NaCl + 0.003 M Ce(NO3)3 solution. In this part, the experiments were performed by repeatedly observing an identical location on the specimens exposed to the studied solution
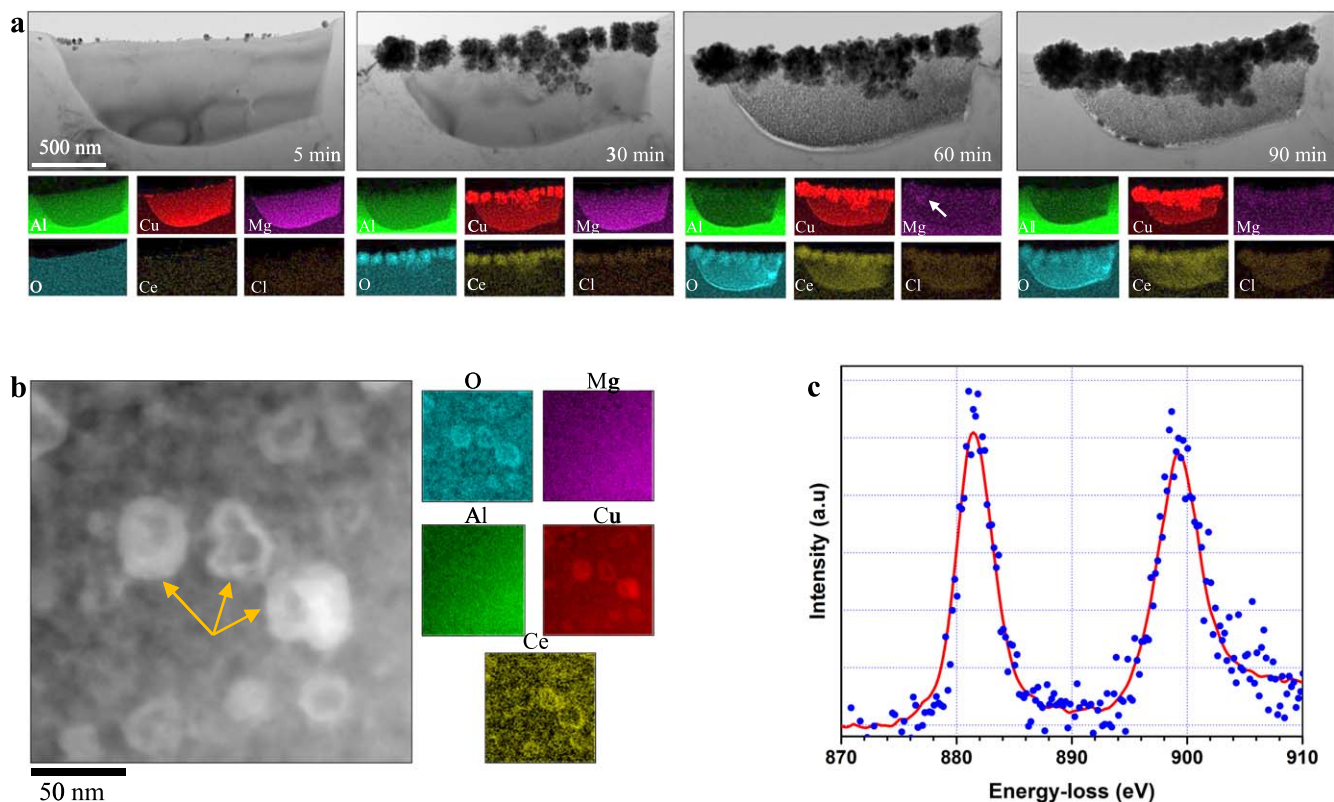
Figure 2. Quasi in situ studies of S-phase inhibition. (a) Time-resolved TEM images and the corresponding EDS maps of an Al_2CuMg particle intermittently exposed to 0.01 M NaCl + 0.003 M $Ce(NO_3)_3$. (b) High angle annular dark field (HAADF)-STEM/EDS analysis of Al_2CuMg particles exposed to the same solution for 40 min, revealing the discretely-deposited cerium at the Cu-rich rims. (c) EEL-spectrum collected from the S-phase particle in Fig. 2a after 90 min; the red curve represents the MLLS fitting to the experimental dots.

outside the electron microscope. After each exposure event, the specimens were rinsed off with distilled water for a few seconds. Then, water on the specimens was immediately absorbed by delicate-task wipes and the specimens were dried under a lamp, followed by plasma-cleaning right before re-inserting into the TEM column. Cross-sectional TEM investigations were carried out on the polished AA2024-T3 sheets exposed to the same solution for different exposure times of 1.5, 6, 24 and 96 h. After completion of the exposure, the samples were rinsed off with distilled water for a few seconds to avoid direct salt precipitation upon drying. The surface morphology of IMPs was examined initially with secondary electron scanning electron microscopy/energy dispersive spectroscopy (SEM/EDS) and then the thin cross-sections were fabricated out of the IMPs of interest with a Thermo-Fisher Helios G4 focused ion beam/scanning electron microscope (FIB/SEM). A Tecnai F20ST/STEM 200 kV equipped with an Oxford Instruments X-MaxN 100TLE windowless detector and a high-resolution Gatan imaging filter (GIF) were employed to perform typical (scanning) TEM imaging, EDS, electron energy loss (EEL) spectroscopy and energy-filtered TEM. To do elemental mapping on the samples, EDS and EF-TEM analysis were conducted. The latter was obtained by filtering $Ce-M_{3,4}$ and $Cu-L_{2,3}$-edge using 30-eV and 20-eV slits, respectively. The EEL-spectra of cerium were collected at an energy resolution of 0.9 eV and energy dispersion of 0.1 eV pixel^{-1}. Multiple linear least-squares (MLLS) fitting was used to fit the reference spectra of Ce(III) and Ce(IV) to the collected spectra, distinguishing the oxidation state of the cerium deposit at different exposure times.[35] Prior to the fitting process, the background signal was subtracted from the spectra using the power-law model. Subsequently, to remove the possible impact of plural scattering on the fitting results, the log-ratio method using the zero-loss peak of the corresponding spectra was applied.[36]

Results and Discussion

Electrochemical and morphological of the alloy surface during exposure.—Figure 1a shows the OCP and LPR values recorded for AA2024-T3 continuously exposed to the studied solution. During the first 1.5 h of exposure, we see the corrosion potential of the sample going up from −510 to −460 mV. In the same course of the exposure, the LPR plot shows an increase from 45 to 85 kΩ in value, although an initial drop of 15 kΩ is distinguishable from 15 min to 30 min. Up to this point, the top-view SEM/EDS examinations (Fig. 1b; the corresponding EDS spectra are partly shown in Supplementary Materials) show no clear indication of cerium precipitation, although the evolving electrochemical response (i.e., OCP and LPR values) implies the occurrence of nanoscopic events that cannot be revealed here due to the limited resolution of SEM. Prolonged exposure up 6 h causes a gradual increase and decrease in the OCP and LPR values, respectively. The OCP value reaches approximately −440 mV while the LPR steeply goes down to 30 kΩ and then starts to slowly increase to 45 kΩ. At this stage, the S-phase particles reveal an obvious change in contrast associated with cerium (hydr)oxide precipitation confirmed by EDS analysis (see Supplementary Materials) while we observe no clear alteration to the other types of IMPs.

From 6 to 24 h, the OCP and LPR values steeply increase to −330 mV and 160 kΩ. Up until 24 h, we observe more S-phase particles significantly covered with the cerium-based precipitate. Besides, θ-phase indicates a sign of interaction with the environment as the contrast has slightly changed on some of the particles. At this stage, we still cannot distinguish any change to the constituent phase particles. From this stage on, the inhibited system stabilises as both the OCP and LPR values show plateaus at around −350 mV and 300 kΩ, respectively. The SEM image shows several pits on the surface that are probably left behind by the fallen-out S-phase particles since
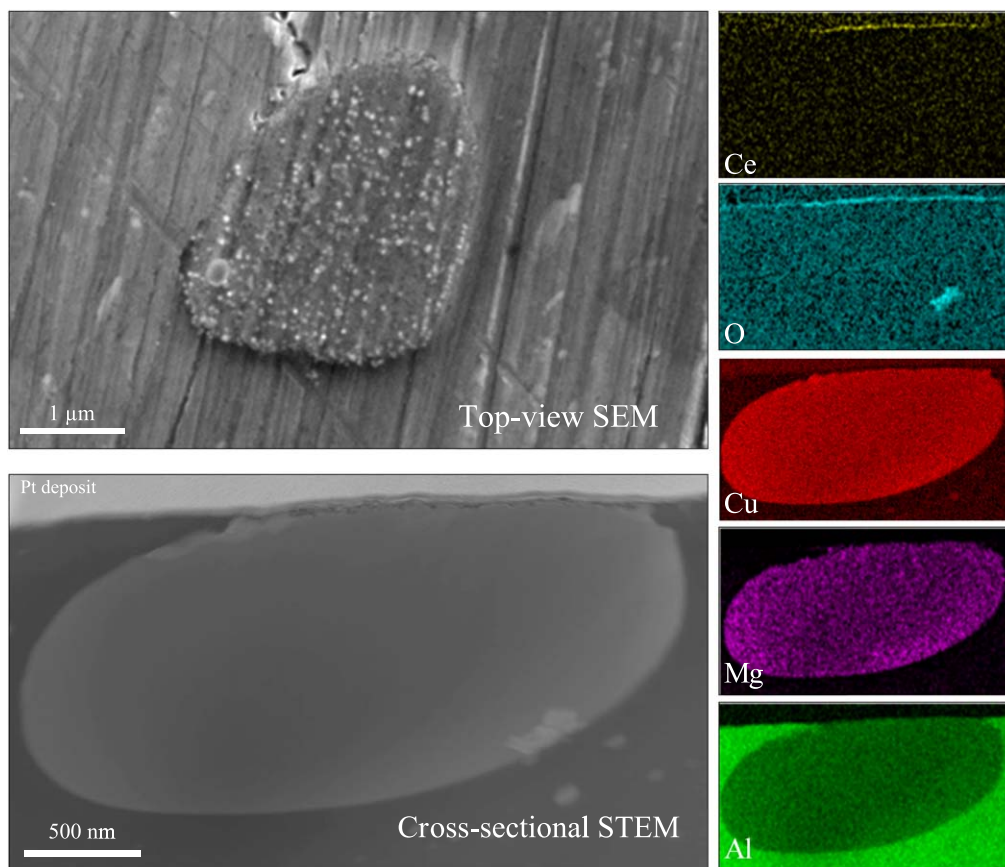
Figure 3. Post-mortem analysis of exposed S-phase particles after 1.5 h. Top-view SEM and cross-sectional STEM/EDS analysis of an Al_2CuMg particle on an AA2024-T3 sheet exposed to 0.01 M NaCl + 0.003 M $Ce(NO_3)_3$. The cross-section has been prepared with FIB. Mind that there is a Pt layer deposited over the particle to protect it from Ga damage while milling.

we comparatively found a lower number of surface S-phase particles at this stage. Furthermore, the θ-phase particles look completely darker in contrast, appearing in a nodular morphology, while most of the constituent phase particles seem bare until 96 h of exposure (mind the representative corresponding SEM images).

Nanoscopic examinations of exposed isolated IMPs.—Nanoscopic investigations are needed for a detailed understanding of the link between the morphological and compositional evolution to the corresponding electrochemical response of the alloy during exposure. Therefore, in this part, we perform analytical TEM measurements over individual IMPs in AA2024-T3 exposed to 0.01 M NaCl + 0.003 M $Ce(NO_3)_3$ solution for different exposure times.

S-phase (Al_2CuMg).—Figure 2 shows quasi in situ STEM/EDS analysis of an Al_2CuMg particle. A 5-min exposure slightly evolves the particle as compared to the fresh condition (not shown here). A few Cu nanoparticles appeared at the edge likely due to the dealloying of the upper thin part (mind the corresponding Cu map). At this stage, we detected no clear cerium precipitate on any region and the particle still contains considerable amounts of aluminium and magnesium. At the total exposure of 30 min, we observe nano-aggerates grown at the edge of the particle where the copper nanoparticles were formed initially. The EDS maps reveal that these are Cu-rich regions that can partly be sourced from the corroded nanometric Cu-containing IMPs that undergo dealloying and release copper in a shorter time scale. Given the aluminium and magnesium map, we see that dealloying has occurred to this region whilst the rest of the particle is still intact. At this stage, we merely detect cerium on the Cu-rich region and not on the intact part of the

particle. This phenomenon suggests the Cu-rich regions as the main sites for cathodic activities, leading to the required alkalinity for the cerium precipitation. This has further been investigated by studying another S-phase particle shown in Fig. 2b. As can be seen, the dealloying has led to the formation of Cu-rich regions over an S-phase particle; however, cerium has just been detected around these regions as discrete islands. With prolonged exposure (i.e., towards 60 min exposure time in total), we see that the nano-aggregates have further grown, associated with dealloying of the entire particle and trenching of the adjacent alloy matrix. The EDS maps show that the particle is depleted in aluminium and magnesium, although the latter is still found in some regions where the highest alkalinity is expected (note the white arrow in the Mg map). During the next 30 min exposure (i.e., towards 90 min exposure time in total), the particle changes slightly in terms of cerium precipitation; however, some Cu-aggregates apparently attached to the matrix appear in the trench. They can actually be the redeposited copper, resulting from a process occurring right after the particle detachment from the alloy matrix.[33] Besides, the EEL-spectrum collected from the particle and fitted to the reference spectra reveals that the deposited cerium, at this stage, has the valency of three (Ce(III)). This implies that the initial cerium precipitates as a direct consequence of alkalisation by the cathodic activities, herein, Cu-rich regions.

Figure 3 shows an Al_2CuMg particle on an AA2024-T3 sheet exposed for 1.5 h. As can be seen in the top-view SEM image, there is no clear indication of cerium precipitation at this stage while bright nanoscopic spots are observed on this particle. The cross-sectional STEM image reveals that the top part of the particle has slightly been dealloyed and this has been associated with precipitation of a narrow layer of cerium (hydr)oxide as shown in the oxygen map. Top-view SEM in Fig. 4 reveals an S-phase particle that is
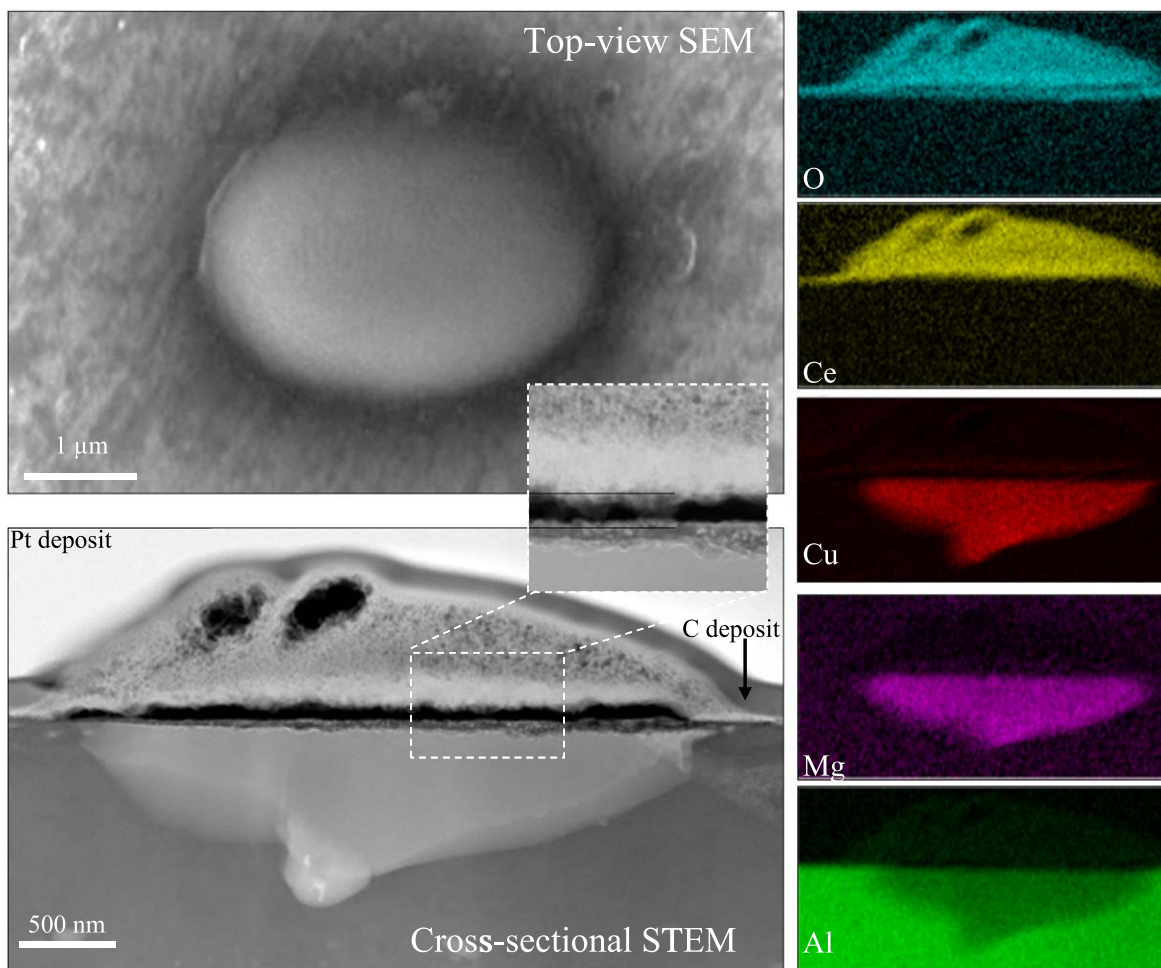
Figure 4. Post-mortem analysis of exposed S-phase particles after 6 h. Top-view SEM and cross-sectional STEM/EDS analysis of an Al$_2$CuMg particle on an AA2024-T3 sheet exposed to 0.01 M NaCl + 0.003 M Ce(NO$_3$)$_3$. The inset is the magnified view of the rectangular region on the particle. The cross-section has been fabricated with FIB. Mind that there is a thin layer of carbon followed by Pt deposition on the particle to protect it from Ga damage while milling.

fully covered with a cerium-based layer after 6 h. The STEM image taken from the corresponding cross-section reveals the formation of a thick precipitate on the particle which is slightly extended to the adjacent matrix, although the cerium cap is highly porous. As can be seen, the cerium layer is also present over the adjacent alloy matrix. Interestingly, the dealloying has shallowly penetrated into the particle while there is no indication of the alloy matrix dissolution. It seems that the cerium layer is unable of inhibiting not only the initial dealloying of S-phase but also corrosion propagation into the depth of the corroding particle. This phenomenon has further been evidenced in Fig. 5, showing an S-phase particle on the sample exposed for 6 h. The top-view SEM image shows a fully covered S-phase particle with the cerium-based precipitate. However, the SEM image when the stage is tilted at 52° reveals a gap between the cerium cap and the alloy substrate (Fig. 5b). This implies that at this stage, the underlying environment is not fully insulated from the bulk solution. Looking at the cross-sectional SEM image of this particle (Fig. 5c), we find the cerium layer quite porous and probably unable of particle protection as dealloying has penetrated relatively deep at some locations. Figure 5d shows a closer look at the deep dealloyed region in this particle, indicated by the dashed rectangle. The STEM image reveals the formation of a nanoporous morphology as a consequence of dealloying. Given the corresponding elemental map, we observe the preferential dissolution of aluminium and to a larger extent magnesium from the particle, associated with the rearrangement of copper in a nanoporous morphology. In addition, we have detected chlorine as an indication of the chloride attack responsible for corrosion, here dealloying. Interestingly, the

cerium has just been detected at the top of the particle and not within the dealloyed regions. Cathodic reactions taking place at the upper Cu-rich part of the particle where oxygen is readily available to provide the required alkalinity for the cerium precipitation. However, the propagation of corrosion into the depth (here dealloying) causes an acidic environment, due to metal ion hydrolysis, in which cerium is stable in its soluble ionic state.

Prolonged exposure of the AA2024-T3 to 0.01 M NaCl + 0.003 M Ce(NO$_3$)$_3$ comes along with a change in the corrosion-attack morphology of S-phase particles. Figure 6 shows top-view SEM and cross-sectional STEM/EDS analysis of an S-phase particle. The top-view image reveals the particle and its adjacent alloy matrix covered by the cerium (hydr)oxide layer (bright region) where a circumferential trench is distinguishable as a dark ring at particle/matrix interface. The cross-sectional STEM shows a rather dense cerium layer that has undergone rupture at the trench location. The remnant is fully dealloyed but not undercut, revealing a nano-porous morphology. The elemental map of the rectangular region found the particle enriched in copper but depleted in magnesium and aluminium. Besides, the Ce map clearly demonstrates the presence of a rupture where interestingly a thin layer of aluminium (hydr)oxide has emerged over the cerium cap. This phenomenon is well clear in the corresponding elemental Al and O maps.

Further investigations have been performed on another S-phase particle exposed for 24 h. The cross-sectional TEM image (Fig. 7a) shows a fully dealloyed particle where its surrounding matrix has been trenched too. As can be seen, it seems that a part of the cerium precipitate has been dissolved where a string of corrosion products is
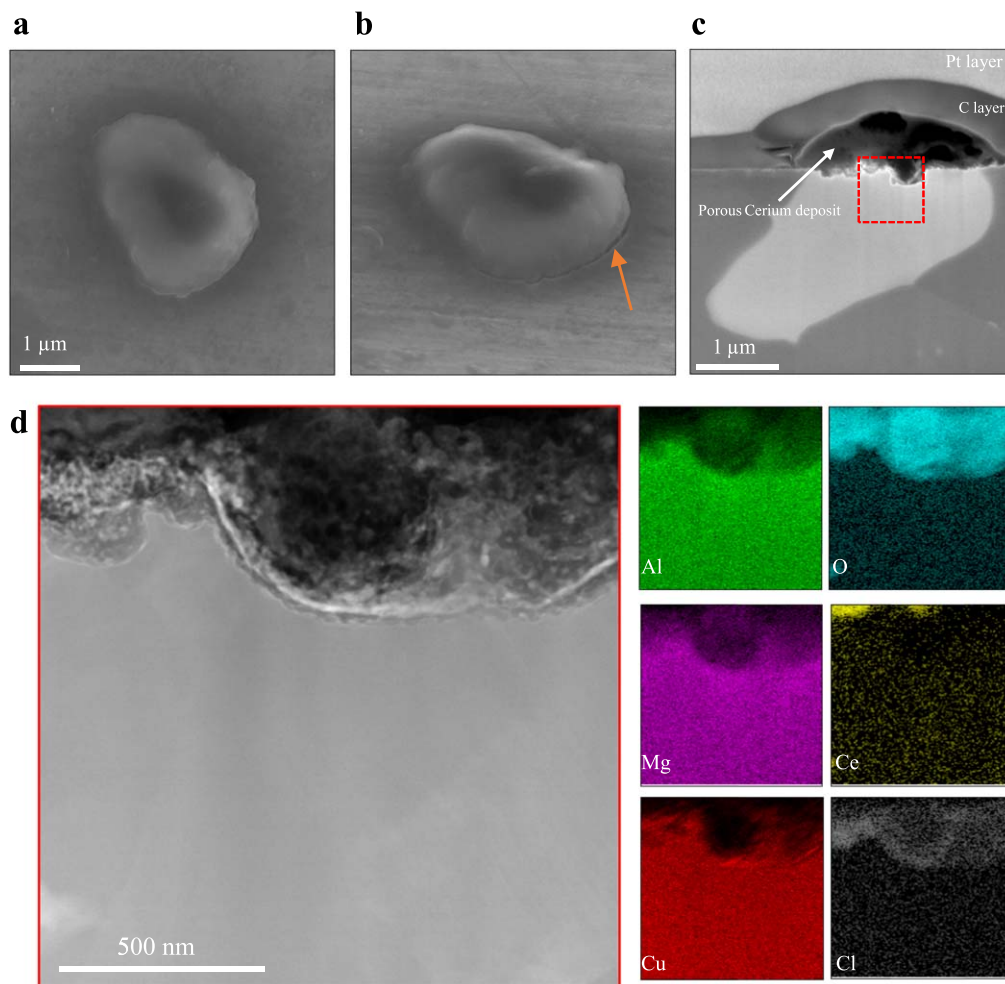
Figure 5. Post-mortem analysis of exposed S-phase particles after 6 h. (a) Top-view SEM of an Al_2CuMg particle on an AA2024-T3 sheet exposed to 0.01 M NaCl + 0.003 M $Ce(NO_3)_3$. (b) SEM image of the particle when the stage is tilted at 52°; the orange arrow indicates the gap between the alloy surface and cerium layer. (c) Cross-sectional SEM image of the same particle; the white arrow denotes the porous cerium layer. (d) STEM/EDS analysis of the rectangular region shown in Fig. 5c. The cross-section has been fabricated with FIB. Mind that there is a thin layer of carbon followed by Pt deposition on the particle to protect it from Ga damage while milling.

observed. The STEM/EDS analysis of this region is shown in Fig. 7b. The STEM image reveals the nano-porous morphology of the S-phase remnant where we see a cerium cap covering both the particle and its adjacent alloy matrix. The white arrow indicates the corrosion products, identified as aluminium (hydr)oxide, that are about to rupture the cerium layer. The EDS analysis reveals a thin Mg-rich layer on the top of the particle, although the particle contains almost no magnesium. It should be noted that this is just a thin FIB section of the whole particle and the rupture has happened at some regions of the cerium precipitate. That is why the cerium layer has been covered by aluminium (hydr)oxide. Figure 7c shows the EEL-spectrum collected from the particle and fitted to the reference spectra. The fitting result indicates that the precipitated cerium on this particle has a Ce(IV)/Ce(III) ratio of 14%. This implies that the transformation of Ce(III) to Ce(IV) is time-dependent as reported by other researchers.[23,37,38] Hydrogen per-oxide (H_2O_2) as an oxidising agent can be responsible for the Ce (III)-to-Ce(IV) transformation as its presence has recently been shown as a consequence of oxygen reduction.[39] Besides, the oxidation of Ce(III) can take place directly over the Cu-rich particle where the solution pH and potential can be high enough; mind the E-pH diagram for cerium.[25]

Figure 8 shows the FIB/SEM 3D reconstruction of an S-phase particle on an AA2024-T3 exposed for 24 h. Figure 8a reveals a buried S-phase remnant and its adjacent alloy matrix covered by a thick layer of cerium (hydr)oxide layer. The location at which the breakdown has occurred is indicated from side- and bottom-view by the white and black arrows in Figs. 8b and 8c, respectively. Top-view 3D reconstruction when the cerium-based cap is removed reveals the circumferential corrosion of the alloy matrix surrounding a dealloyed S-phase remnant (Fig. 8d). As evident in Fig. 8e, the corrosion pit is left behind as a consequence of the alloy matrix trenching. This implies although the S-phase particles are mostly buried under a thick layer of cerium (hydr)oxide, dealloying and trenching corrosion take place underneath and eventually result in pitting corrosion.

θ-phase (Al_2Cu).—Ex situ analytical TEM analysis was per-formed on individual θ-phase particles in AA2024-T3 sheets exposed for different exposure times. Figure 9 shows an Al_2Cu particle exposed to 0.01 M NaCl + 0.003 M $Ce(NO_3)_3$ for 6 h. The top-view SEM reveals several bright spots discretely on the particle; however, there is no indication of significant cerium precipitation at this stage. The STEM/EDS analysis of the corresponding cross-section along the red dashed line reveals local precipitation of cerium on this particle. In fact, we observe cerium precipitation merely and discretely at Cu-rich locations on the particle. Here, the EDS analysis identifies the hills on the particle as $Al(OH)_3$ where the copper aggregates are formed in close vicinity (mind the elemental maps). As we have recently reported, corrosion initiates at θ-phase
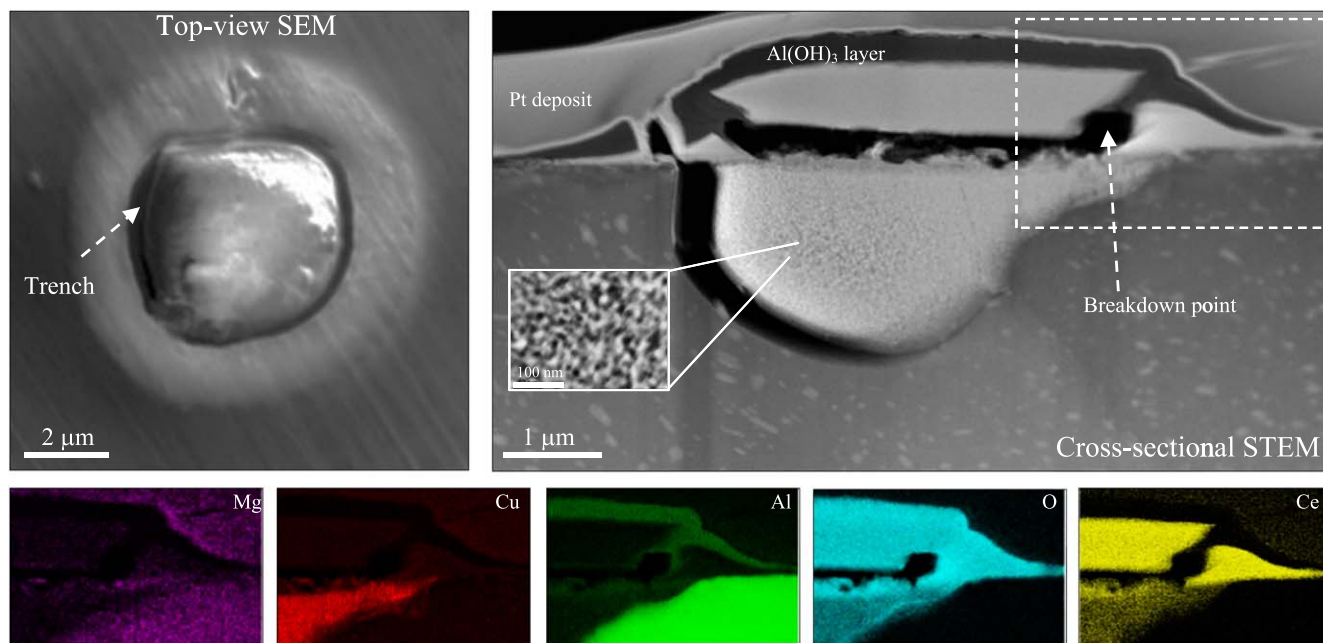
Figure 6. Post-mortem analysis of exposed S-phase particles after 24 h. Top-view SEM and cross-sectional STEM/EDS analysis of an Al_2CuMg particle on an AA2024-T3 sheet exposed to 0.01 M NaCl + 0.003 M $Ce(NO_3)_3$. The inset is the magnified STEM image revealing the nanoporous morphology of the dealloyed remnant. The elemental maps correspond to the rectangular region shown in the STEM image. The cross-section has been fabricated with FIB; mind that there is a Pt layer deposited to protect the particle from Ga damage while milling.
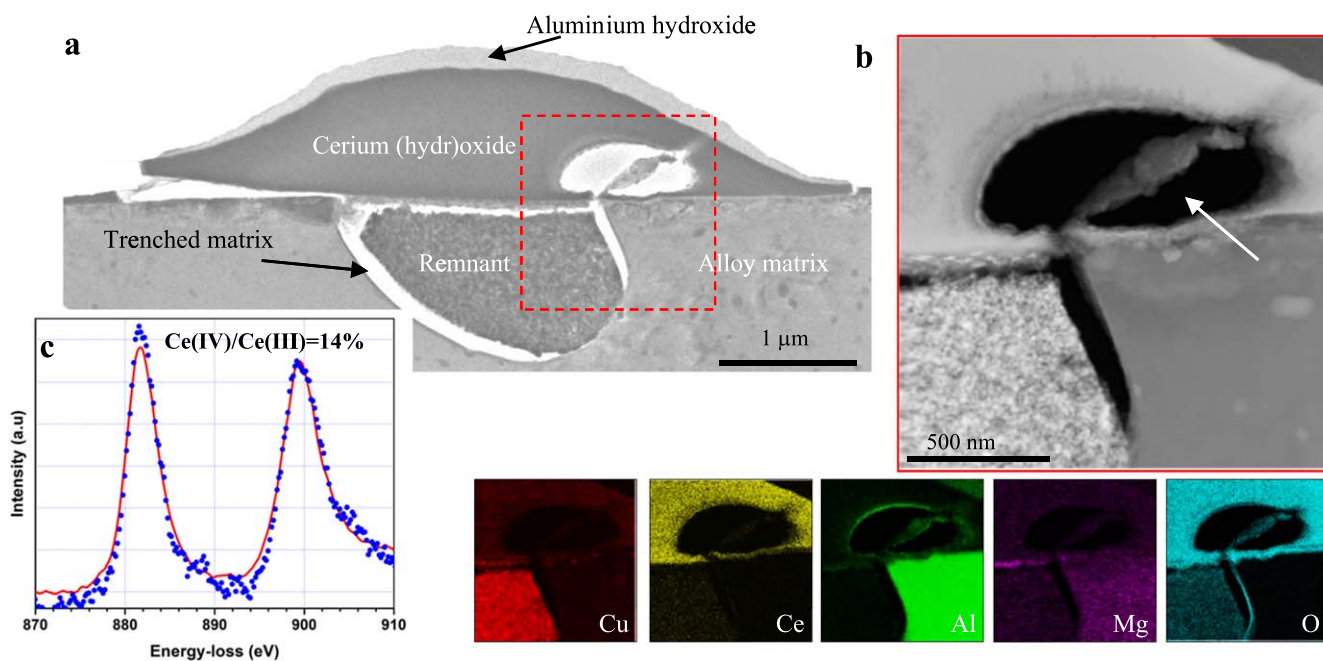

Figure 7. Post-mortem analysis of exposed S-phase particles after 24 h. (a) Cross-sectional TEM image of an Al_2CuMg particle on an AA2024-T3 sheet exposed to 0.01 M NaCl + 0.003 M $Ce(NO_3)_3$. (b) STEM/EDS analysis of the rectangular region shown in Fig. 7a. The white arrow shows the corrosion products while leaving the trenched area. (c) EEL-spectrum collected from the particle; the red curve represents the MLLS fitting to the experimental dots. A Ce (IV)/Ce(III) ratio of 14% was estimated by the MLLS fitting of experimental dots.

particles as a direct consequence of dealloying, leading to the selective dissolution of aluminium and accumulation of copper.[33] In fact, the Cu-rich regions are potential cathodic sites around which alkaline local solution chemistry is expected, triggering the cerium precipitation.

Prolonged exposure for 24 h comes along with a clear change in the top-view morphology of θ-phase particles. The top-view SEM image shown in Fig. 10 reveals a nodular layer on an Al_2Cu particle. The cross-sectional STEM/EDS analysis shows that the hills are in fact $Al(OH)_3$. A closer look at those regions reveals that they are formed merely in close vicinity of the dealloyed segments of the particle. The STEM image shows the occurrence of dealloying gradually penetrating in-depth. This is well clear in the elemental maps, proving selective dissolution of aluminium and local precipitation of cerium.
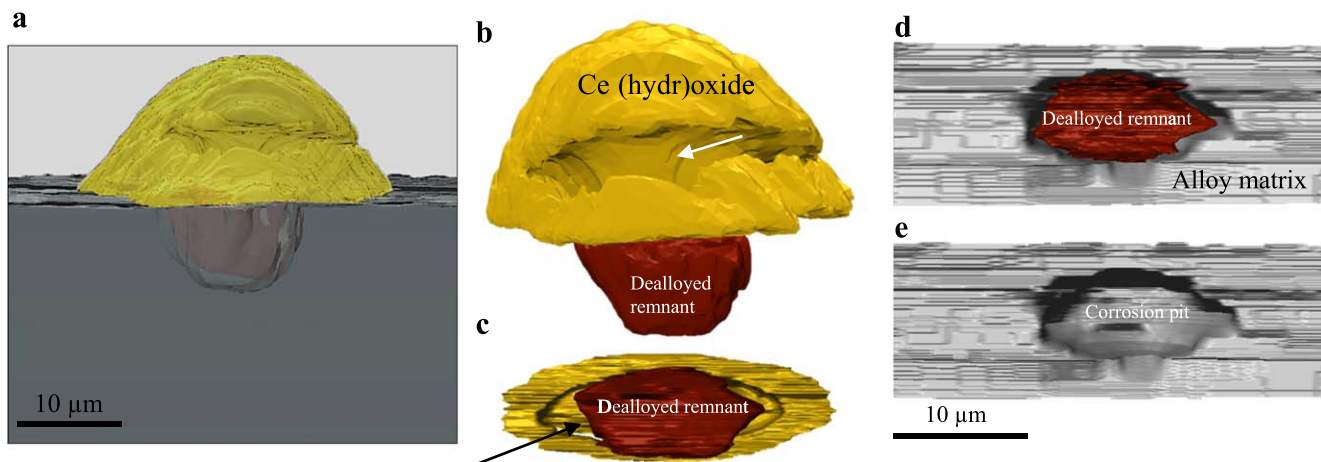
Figure 8. 3D FIB/SEM reconstruction of an S-phase particle after 24 h. (a) 3D reconstruction of the full system including the dealloyed particle, cerium (hydr)oxide precipitate and adjacent alloy matrix. (b) 3D reconstruction from the side-view when the alloy matrix is removed. The white arrow shows the ruptured part of the cerium-based cap. (c) 3D reconstruction from bottom-view when the alloy matrix is removed. The black arrow shows the ruptured part of the cerium-based cap. (d) Top-view 3D reconstruction when the cerium-based cap is removed. (e) Top-view 3D reconstruction when both the cerium (hydr)oxide layer and dealloyed particle are removed, revealing the corrosion pit formed as a consequence of the alloy matrix trenching.
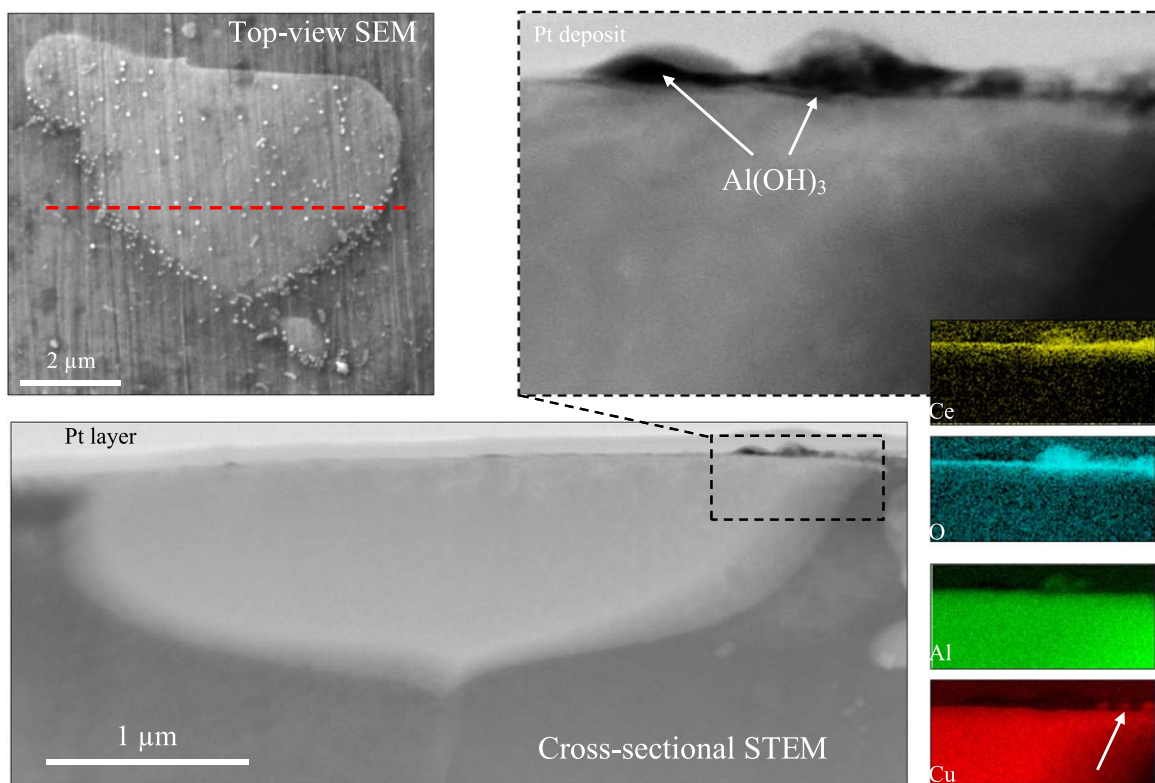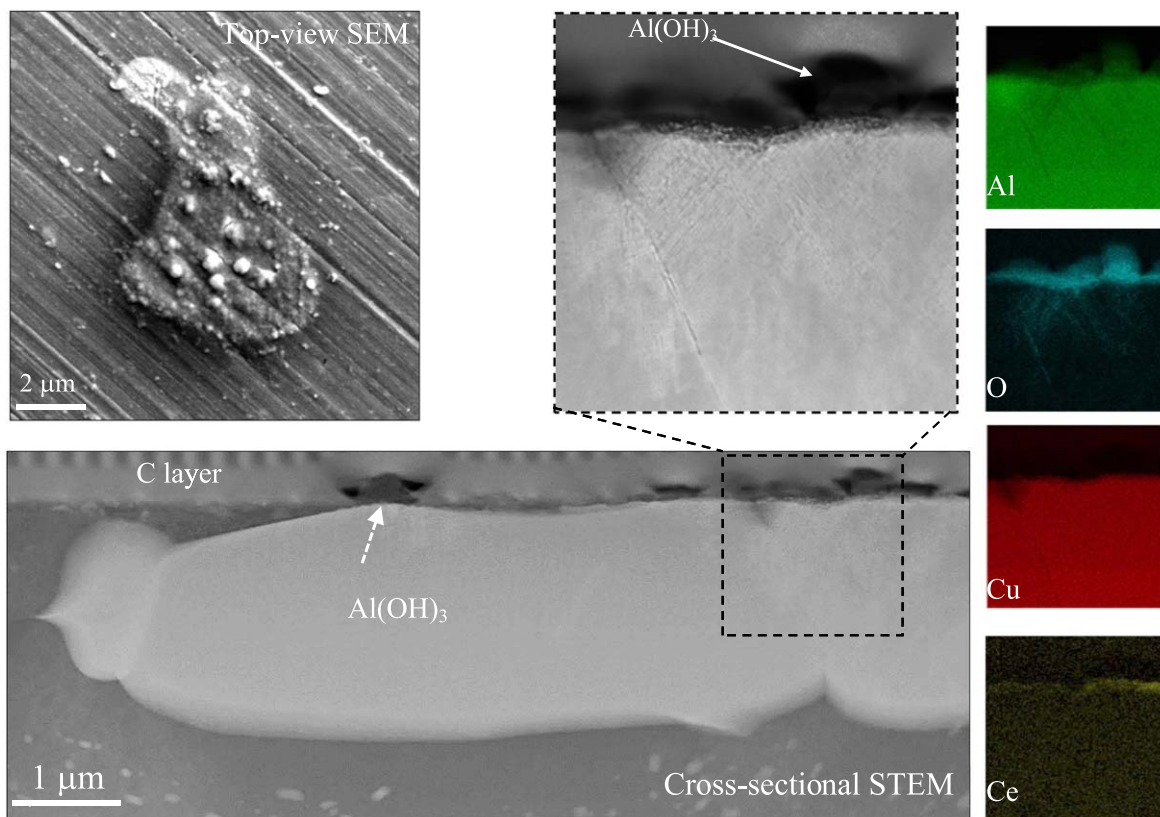

Figure 9. Post-mortem analysis of exposed θ-phase particles after 6 h. Top-view SEM and cross-sectional STEM/EDS analysis of an Al_2Cu particle on an AA2024-T3 sheet exposed to 0.01 M NaCl + 0.003 M $Ce(NO_3)_3$. The elemental maps correspond to the rectangular region shown in the STEM image. The cross-section has been fabricated with FIB; mind that there is a Pt layer deposited to protect the particle from Ga damage while milling.

A coarse nodular morphology is observed once θ-phase particles are exposed for a longer exposure time (i.e., 96 h). In Fig. 11, the top-view SEM image shows a covered Al_2Cu particle surrounded by a trench with a tight opening. The cross-sectional STEM image reveals a nano-porous morphology caused by dealloying where the adjacent alloy matrix has been fully trenched. The EDS analysis shows that the particle is depleted in aluminium while a thin mixed layer of cerium (hydr)oxide and aluminium (hydr)oxide is observed on the top. The Ce(IV)/Ce(III) ratio of 8% within the deposit is estimated by MLLS fitting of the collected spectrum. Compared to S-phase, the cerium deposit is rather thin on the θ-phase particle.

Like for S-phase, it seems that cerium cannot inhibit dealloying of Al_2Cu particles and dealloying eventually occurs in both phases. As we recently reported, dealloying of θ-phase takes place over a longer time of exposure as it is electrochemically more stable than S-phase.[33] Here, the faster dealloying probably leads to a higher rate of cerium precipitation. In fact, the dealloying rate seems to be accountable for establishing the required local chemistry required for cerium precipitation; this phenomenon will be discussed later.

Constituent phases ($Al_7Cu_2Fe(Mn)$, $Al_{76}Cu_6Fe_7Mn_5Si_6$).—We studied a variety of particles at exposure times of 1.5, 6 and 24 h

Figure 10. Post-mortem analysis of exposed θ-phase particles after 24 h. Top-view SEM and cross-sectional STEM/EDS analysis of an Al_2Cu particle on an AA2024-T3 sheet exposed to 0.01 M NaCl + 0.003 M $Ce(NO_3)_3$. The elemental maps correspond to the rectangular region shown in the STEM image. The cross-section has been fabricated with FIB; mind that there is a C layer deposited to protect the particle from Ga damage while milling.

and mostly no indication of cerium interaction with the constituent phases was found (see Supplementary Materials (available online at stacks.iop.org/JES/168/041505/mmedia)). However, our quasi in situ investigations showed that the constituent phases might respond differently to the cerium-containing solution during the exposure. In fact, we detected cerium merely on constituent phase particles that have accommodated redeposited Cu nanoparticles. Otherwise, they show no interaction with the cerium-inhibited solutions in short periods of exposure. For instance, Fig. 12a shows quasi in situ TEM/EFTEM-EELS analysis of an $Al_7Cu_2Fe(Mn)$ particle in an argon ion-milled thin specimen. After 30 min of exposure, we see the appearance of the nanoparticles, identified as elemental copper, on this particle, leading to slight cerium precipitation. Besides, the EELS analysis shows a Ce(IV)/Ce(III) ratio of 0 at this stage. A closer look at these Cu nanoparticles is shown in Fig. 12b. With prolonged exposure until 90 min, we see the nanoparticles slightly growing in size and number and this is associated with slightly more Ce(III) deposited on the particle. After total exposure of 150 min, the particle has been analysed using STEM/EDS, clearly showing the presence of the Cu nanoparticles (Fig. 12c). As expected, the elemental map shows some cerium deposited on the particle around Cu-rich regions. In addition, there are regions on the particle depleted in aluminium, implying the occurrence of dealloying. In a prior work,[33] we have shown that the redeposited Cu nanoparticles commonly originate from the undercut S-phase particles, speeding up the dealloying of constituent phases. It should be noted the Cu redeposition takes place on some of the constituent phases even in the uninhibited solutions (see Supplementary Materials).

Further investigations were carried out ex situ on a variety of particles at exposure times of 1.5, 6, 24 and 96 h. Typically, cerium does not interact with the constituent phases in short periods of exposure in the absence of the redeposited Cu nanoparticles (see

Supplementary Materials). For instance, Fig. 13 shows an $Al_7Cu_2Fe(Mn)$ particle exposed to 0.01 M NaCl + 0.003 M $Ce(NO_3)_3$ for 96 h. The top-view SEM image shows regions having a brighter contrast on the particle whilst no circumferential trenching is observed. The cross-sectional STEM image reveals a few hills identified as $Al(OH)_3$ on the particle. Given the STEM/EDS analysis, we see that the particle has slightly been dealloyed on the top, causing the formation of a thin Cu-rich layer (see the Cu map). The interesting point is that cerium has been discretely deposited at the dealloyed locations.

We have also found $Al_7Cu_2Fe(Mn)$ particles that are covered uniformly with a thin layer of cerium (hydr)oxide. Figure 14 shows the top-view morphology of an $Al_7Cu_2Fe(Mn)$ particle with bright spots all over the particle. Our analysis identified them as copper nano-particles or -clusters deposited mostly on the particle and slightly over the alloy matrix. The cerium map superimposed on the cross-sectional STEM image shows a thin uniform layer of cerium (hydr)oxide on this particle. Interestingly, cerium precipitation is observed at the Cu-rich locations on the alloy matrix as well. The magnified STEM/EDS analysis of the rectangular region clearly reveals that the top surface of the particle has slightly been dealloyed and this is associated with uniform cerium precipitation. This is consistent with quasi in situ TEM results, implying the role of Cu nanoparticles in enhancing cerium precipitation.

Figure 15 shows an $Al_{76}Cu_6Fe_7Mn_5Si_6$ particle exposed for 96 h. The SEM image reveals a bright spot on the particle, although no sign of corrosion attack to its adjacent matrix. Our cross-sectional TEM evaluation reveals that this particle has not interacted with cerium-inhibited solution (Fig. 15b). A closer look at the particle shown in Fig. 15c shows that although the particle has been slightly dealloyed, no cerium peak shows up in the collected EDS spectrum. In fact, $Al_{76}Cu_6Fe_7Mn_5Si_6$ particles are stable phases that sluggishly undergo dealloying during exposure. Thus, the rate of dealloying
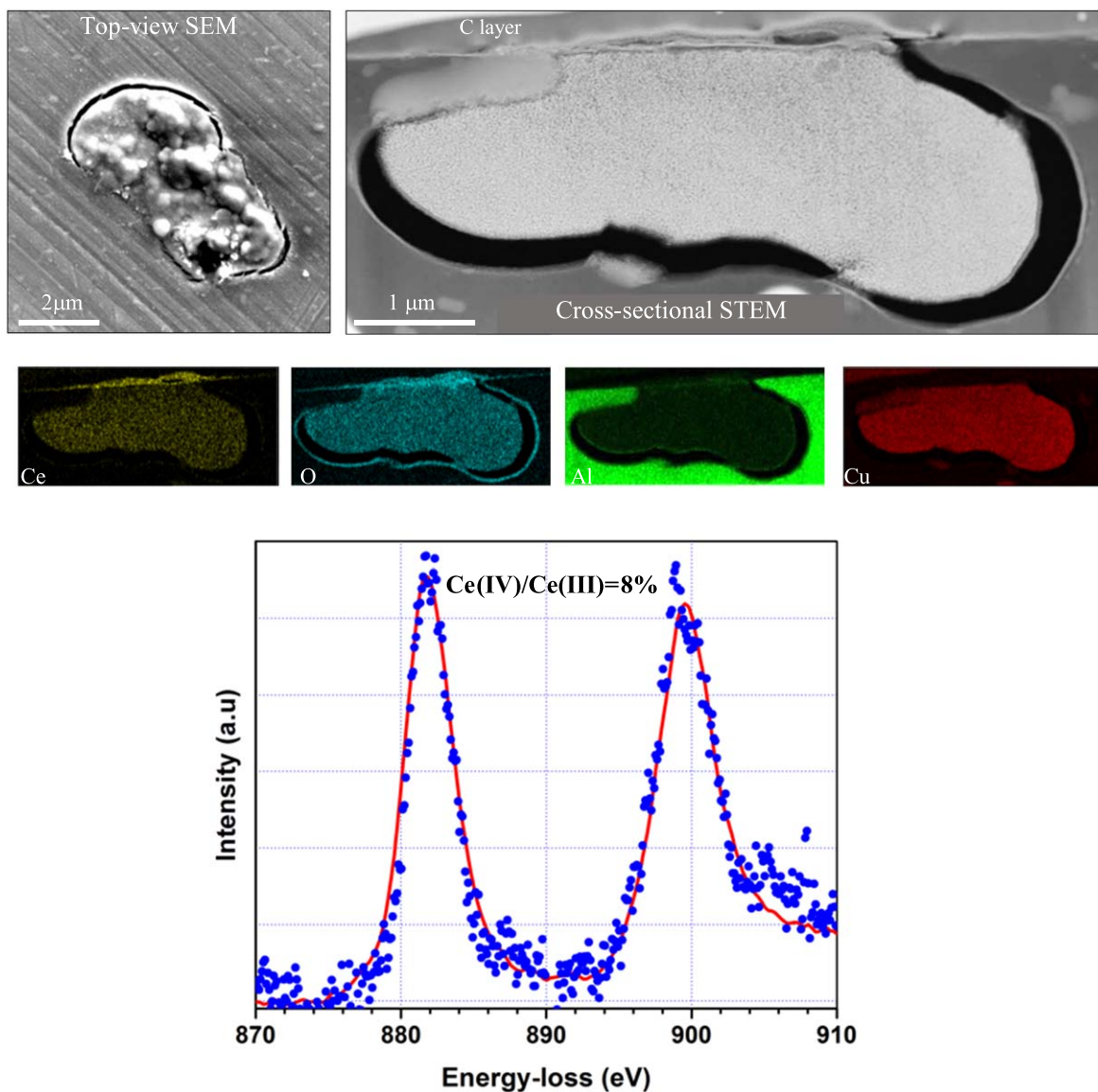
Figure 11. Post-mortem analysis of exposed θ-phase particles after 96 h. Top-view SEM and cross-sectional STEM/EDS analysis of an Al$_2$Cu particle on an AA2024-T3 sheet exposed to 0.01 M NaCl + 0.003 M Ce(NO$_3$)$_3$. The graph is the EEL-spectrum collected from the particle; the red curve represents the MLLS fitting to the experimental dots. A Ce(IV)/Ce(III) ratio of 8% was estimated by the MLLS fitting of experimental dots.

surely seems to have an impact on local solution chemistry which drives the cerium precipitation. This phenomenon will be discussed in the next section.

Local Corrosion Inhibition Mechanism by Cerium-Based Inhibitors

Conventionally, microgalvanic coupling established between isolated IMPs and their surrounding matrix has been proposed as the main cause of local corrosion in aluminium alloys.[40,41] We have recently reported that IMPs are in fact active phases that undergo initial dealloying regardless of their cathodic and anodic types while the microgalvanic coupling takes place between the dealloyed parts of an IMP and its surrounding alloy matrix at moderate stages.[33,34] This phenomenon, in turn, drives local corrosion and further promotes the local solution chemistry around the IMPs. Here, we observed that dealloying is the root cause of cerium precipitation and not microgalvanic coupling. Actually, nanogalvanic coupling within the corroding IMPs induces local solution chemistry that leads to local cerium precipitation. However, the approach used in this study

is unable of determining how alkaline the solution chemistry is around different IMPs. Nevertheless, we know that cerium precipitation can only occur on IMPs when the local pH is sufficiently alkaline. For Al$_2$CuMg particles, the local solution chemistry is probably strongly alkaline as we observe a high rate of precipitation. Besides, if the dealloying stops at some points owing to the cerium-based layer, the local pH decreases and no further precipitation would take place which is the case for constituent phases. In addition, relatively slow but ongoing dealloying happens to Al$_2$Cu particles where the particles of relevance are found to be fully dealloyed but covered with a thin layer of cerium (hydr)oxide. Thus, individual intermetallic particles can experience different local solution chemistry and local corrosion potential that will surely affect the Ce(IV)/Ce(III) ratio as well. For S-phase, stronger local alkalinity and higher corrosion potential due to dealloying can lead to a higher Ce(IV)/Ce(III) ratio, compared to other intermetallic phases. Furthermore, the oxidation of Ce(III) to Ce(IV) by H$_2$O$_2$ is time-dependent; therefore for Al$_2$Cu and constituent phase intermetallic particles which get involved in the cerium deposition process later, a lower Ce(IV)/Ce(III) ratio can be considered
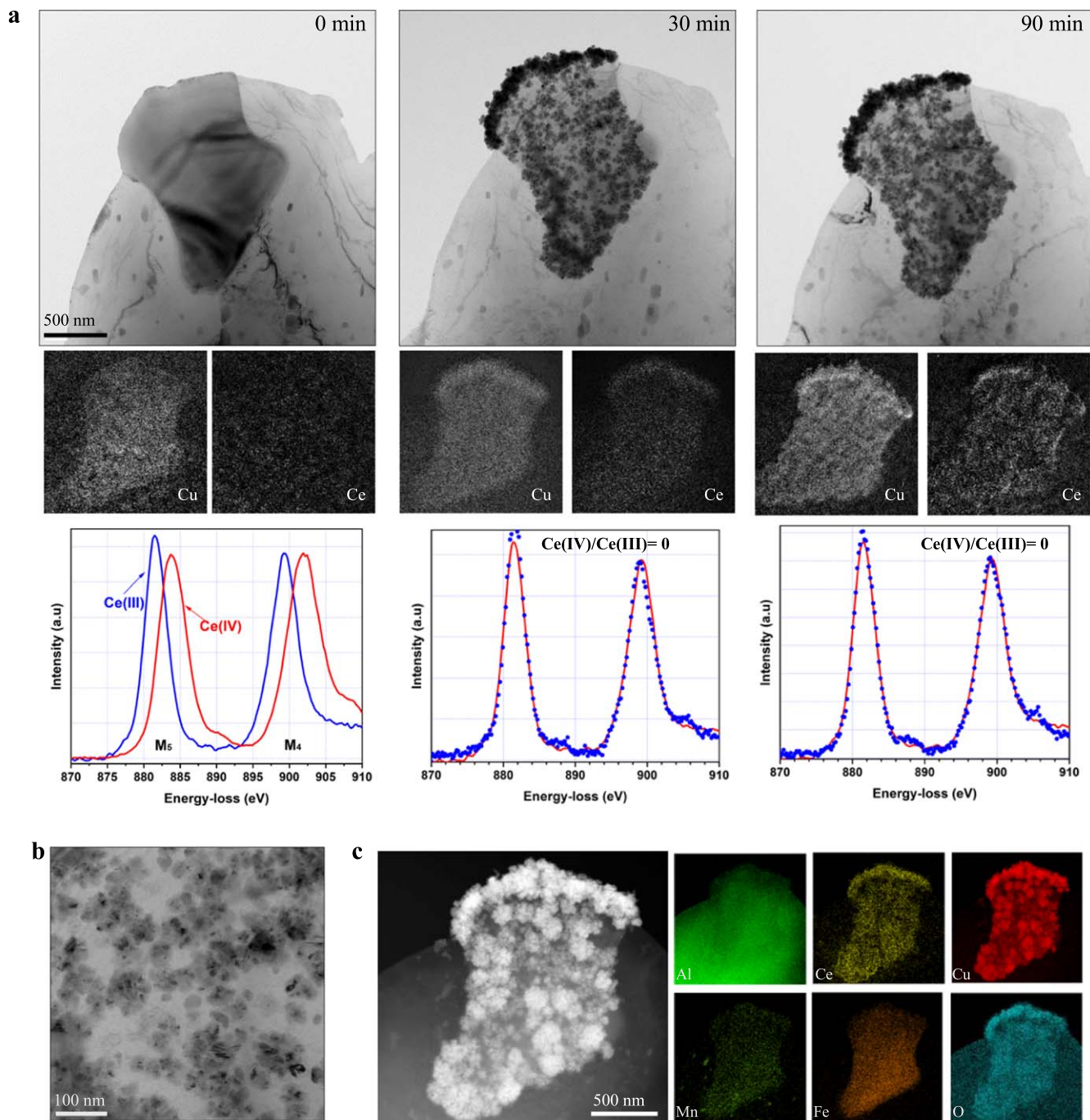
**Figure 12.** Quasi in situ studies of $Al_7Cu_2Fe(Mn)$ inhibition. (a) Quasi in situ TEM/EFTEM-EELS study of an $Al_7Cu_2Fe(Mn)$ particle exposed to 0.01 NaCl + 0.003 $Ce(NO_3)_3$ at different exposure times. EELS spectra were collected from the particle at each exposure time. Cerium and copper were mapped using energy-filtering the corresponding edges in the EELS spectra. The graphs at 0 min exposure are reference spectra of Ce(III) and Ce(IV). The collected spectra were MLLS fitted to the reference spectra. (b) A closer look at the particle after 30 min exposure shows the redeposited Cu nanoparticles. These particles can accelerate dealloying of the particle so that the environment reach enough alkalinity for Ce precipitation. (c) STEM/EDS image of the particle after 150 min clearly proves the presence of cerium oxide islands around the Cu nanoparticles.

reasonable. We further discuss the impact of cerium precipitation on morphological and compositional evolutions of different individual intermetallic phases.

Inhibition mechanism of S-phase.—Al_2CuMg particles are highly active and undergo dealloying at a relatively fast rate.[33] The initial selective dissolution of aluminium and magnesium results in the formation of copper-rich regions on the S-phase particles that can support cathodic reactions through a nanogalvanic coupling.

This phenomenon gradually established a very local alkalinity that is required for cerium precipitation. We have already proved that all the anodic and cathodic reaction will take place on one single particle at early stages.[33] At this stage, the cerium precipitation cannot inhibit dealloying and it progressively propagates into the depth. At moderate stages, the S-phase particle still endures dealloying while oxygen evolution as the cathodic reaction takes place on the Cu-rich top of the particle.[42] This leads to precipitation of a thick but porous cerium cap over the particle and its adjacent alloy
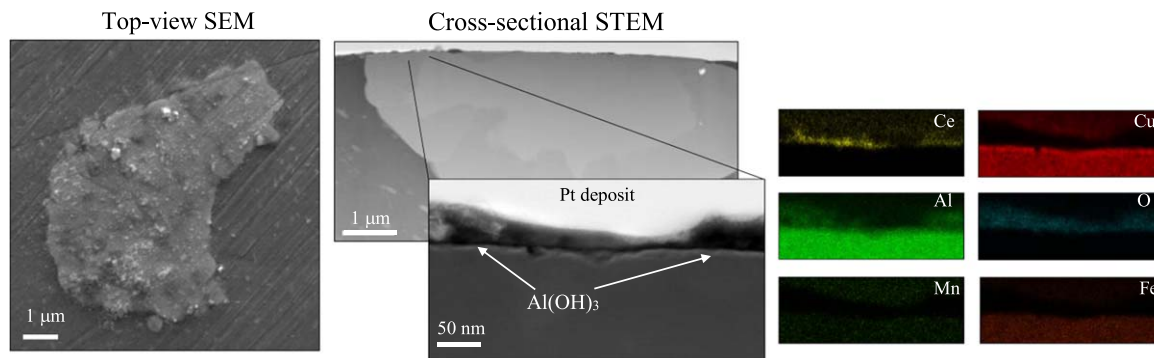
Figure 13. Post-mortem analysis of exposed $Al_7Cu_2Fe(Mn)$ particles after 96 h. Top-view SEM and cross-sectional STEM/EDS analysis of an $Al_7Cu_2Fe(Mn)$ particle on an AA2024-T3 sheet exposed to 0.01 M NaCl + 0.003 M $Ce(NO_3)_3$. The elemental maps correspond to the rectangular region shown in the STEM image. The cross-section has been fabricated with FIB; mind that there is a Pt layer deposited to protect the particle from Ga damage while milling.
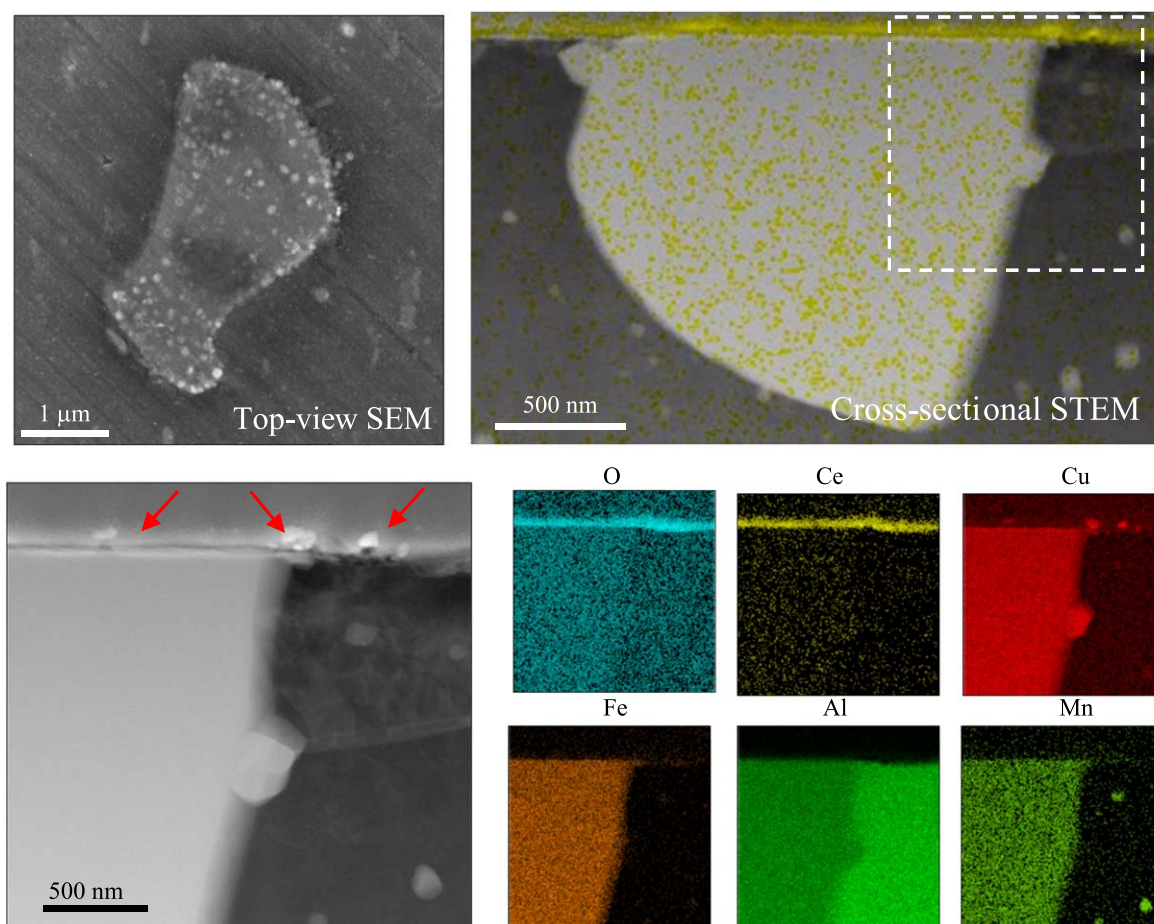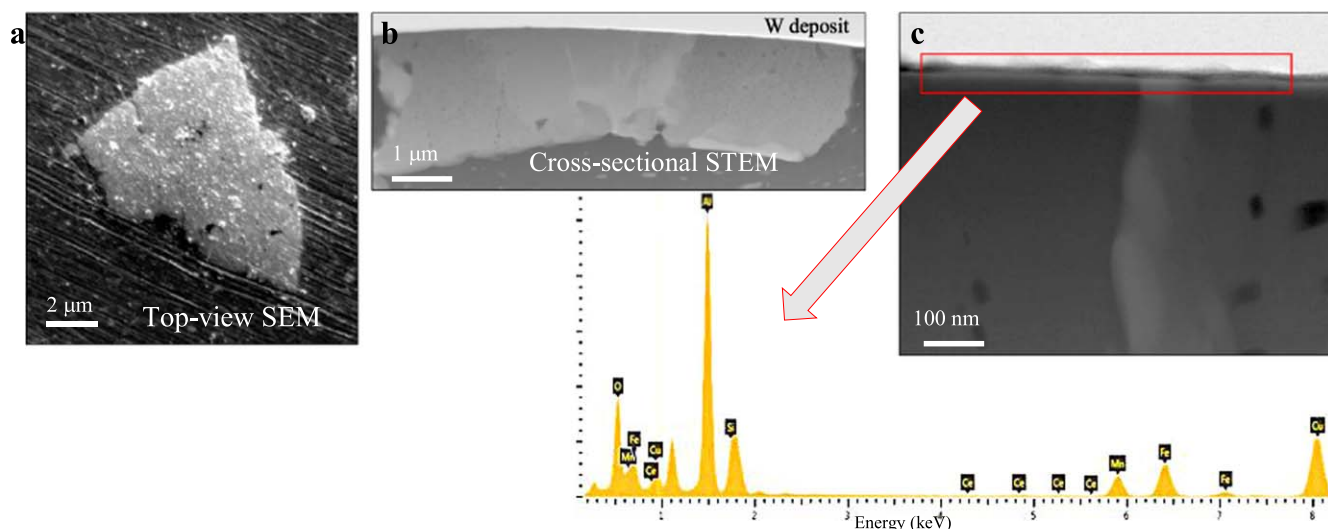

Figure 14. Post-mortem analysis of exposed $Al_7Cu_2Fe(Mn)$ particles after 96 h. Top-view SEM and cross-sectional STEM/EDS analysis of an $Al_7Cu_2Fe(Mn)$ particle on an AA2024-T3 sheet exposed to 0.01 M NaCl + 0.003 M $Ce(NO_3)_3$. The cerium map is superimposed on the STEM image. The elemental maps correspond to the rectangular region shown in the STEM image. The white arrow indicates the Cu nanoparticles deposited on the $Al_7Cu_2Fe(Mn)$ particle and its adjacent matrix. These Cu nanoparticles cause an enhanced cerium deposition. The cross-section has been fabricated with FIB; mind that there is a C layer deposited to protect the particle from Ga damage while milling.

matrix. It should be noted the cerium (hydr)oxides may have relatively low electrical conductivity and the cathodic reaction has to happen beneath the cerium layer.

As the dealloying further penetrates into the particle, the adjacent alloy matrix also gets involved in the process and starts to dissolve circumferentially. Unlike the top part of the particle, there is an acidic environment established in-depth due to metal hydrolysis. In such an environment, aluminium and magnesium are soluble species in water, releasing from the particle and its surrounding matrix. This increasingly leads to the accumulation of corrosion products underneath the cerium precipitate, causing internal pressure. Thus, this gives rise to rupture or partial dissolution of the cerium deposit since cerium (hydr)oxides are thermodynamically unstable in acidic pH values.[25] As soon as the rupture occurs, the soluble species would be released from the trench. Mg ions would diffuse away as they are still soluble in the bulk solution pH. However, Al ions would precipitate as $Al(OH)_3$, covering the cerium precipitate. However, the corrosion still continues to dissolve the surrounding alloy matrix

Figure 15. Post-mortem analysis of exposed $Al_{76}Cu_6Fe_7Mn_5Si_6$ particles after 96 h. (a) Top-view SEM and (b) cross-sectional STEM analysis of an $Al_{76}Cu_6Fe_7Mn_5Si_6$ particle on an AA2024-T3 sheet exposed to 0.01 M NaCl + 0.003 M Ce(NO$_3$)$_3$. (c) The STEM image shows a closer look at the top part of the particle which has slightly been dealloyed. The EDS map collected from the rectangular region shows that no cerium has been precipitated on this particle.

until undercutting the corroding particle. That the S-phase, if covered with the cerium layer, can still liberate some Cu ions into the environment through the ruptured regions of the precipitate. Besides, the undercut might fall out and leave behind surface corrosion pits. During the first 24 h, the electrochemical response of the system is mainly linked to S-phase evolutions. In fact, both the copper enrichment and cerium precipitation cause an increase in OCP and LPR values up to 24 h (see Fig. 1a). Figure 16 schematically shows different stages of cerium interaction with S-phase particles.

Inhibition mechanism of θ-phase.—Al$_2$Cu is also an unstable phase that undergoes dealloying but at a slower rate compared to S-phase. Since dealloying is the main reason for the local solution chemistry establishment, the cerium precipitation rate is rather low on θ-phase particles. In fact, the corrosion initiates by a dealloying attack at several locations on an Al$_2$Cu particle, resulting in the formation Al(OH)$_3$ islands. Furthermore, the Cu-rich islands support cathodic reactions which leads to local alkalinity required for cerium precipitation. However, since the process progress sluggishly, the precipitation rate is rather low compared to S-phase. As time elapses, the Al(OH)$_3$ islands are covered with cerium (hydr)oxide, causing the particle to appear in a coarse nodular morphology. At moderate stages of inhibition, the dealloying continues to penetrate into the particle and this is associated with the corrosion of the adjacent alloy matrix. At this stage, the underlying corrosion speeds up a bit and the top part of the particle is responsible for accommodating cathodic reactions. This gives rise to enhanced local alkalinity on the particle which increases the cerium precipitation rate. The process proceeds further until ending up with an undercut particle which is covered with a thin layer of cerium (hydr)oxide and aluminium hydroxide. It should be mentioned that the whole process from initiation to undercutting takes longer as compared to that for S-phase particles.

Inhibition mechanism of constituent phases.—Al$_7$Cu$_2$Fe(Mn) and Al$_{76}$Cu$_6$Fe$_7$Mn$_5$Si$_6$ are highly stable phases in the studied cerium-inhibited solution. The latter does not interact with the cerium during a 96-h exposure as it gets slightly dealloyed over a long-term exposure and this cannot induce the required alkalinity for cerium precipitation. However, Al$_7$Cu$_2$Fe(Mn) is less stable and it endures the dealloying attack and selective dissolution of aluminium, leading to the formation of Al(OH)$_3$ piles on the particles. At moderate stages of exposure, this comes along with the discrete

precipitation of cerium at the dealloyed locations. However, some Al$_7$Cu$_2$Fe(Mn) particles can endure a transition due to the copper reprecipitation process. In fact, those particles that are located in the vicinity of S-phase particles may accommodate the released Cu ions. The phenomenon can lead to an accelerated dealloying which establishes uniform local chemistry over the corroding particle. The covered particle is well protected as it is firstly stable and secondly buried under a thin layer of cerium (hydr)oxide, enhancing the electrochemical stability of the constituent phase. This process is schematically shown in Fig. 16. It should be mentioned that the interaction of cerium with θ-phase and constituent phases happens rather slow with time; that is why the system evolves slowly and reveals a nearly stable electrochemical response after 24 h of exposure.

Conclusions

We studied the interaction of cerium nitrate with different intermetallic phases in AA2024-T3 using electrochemical evaluations and also quasi in situ and ex situ analytical TEM at different exposure times up to 96 h. We directly evidenced microstructural evolutions of the isolated IMPs during interaction with the inhibited solution. We observed the pivotal role of dealloying in establishing the basic local solution chemistry which triggers cerium precipitation. We here confirm that IMPs, regardless of their conventional categorisation, are in fact simultaneous anodes and cathodes as from the beginning of the exposure. The dealloying is the main factor steering the precipitation rate of cerium: the faster it happens the more cerium precipitates. The Cu-rich regions resulting from the selective dissolution of active elements like magnesium and aluminium support cathodic reactions leading to a local alkalinity.

Al$_2$CuMg as the most unstable phase is found to be covered with a rather thick cerium-based deposit layer. It is established during several stages of interaction with the cerium-inhibited solution. The cerium in fact cannot inhibit dealloying of the S-phase but can delay the process and mitigate the Cu reprecipitation. The precipitation of cerium takes place on S-phase from the beginning of exposure and no nobility inversion happens. As long as the dealloying propagates into depth, the top Cu-rich part of the corroding particles supports cathodic reaction, generating the required alkalinity for cerium precipitation. The rupture of the cerium cap is a phenomenon that occurs at moderate stages of exposure due to the underlying corrosion.

Al$_2$Cu particles also undergo dealloying in the cerium-containing solution; however, a sluggish rate of dealloying results in less cerium
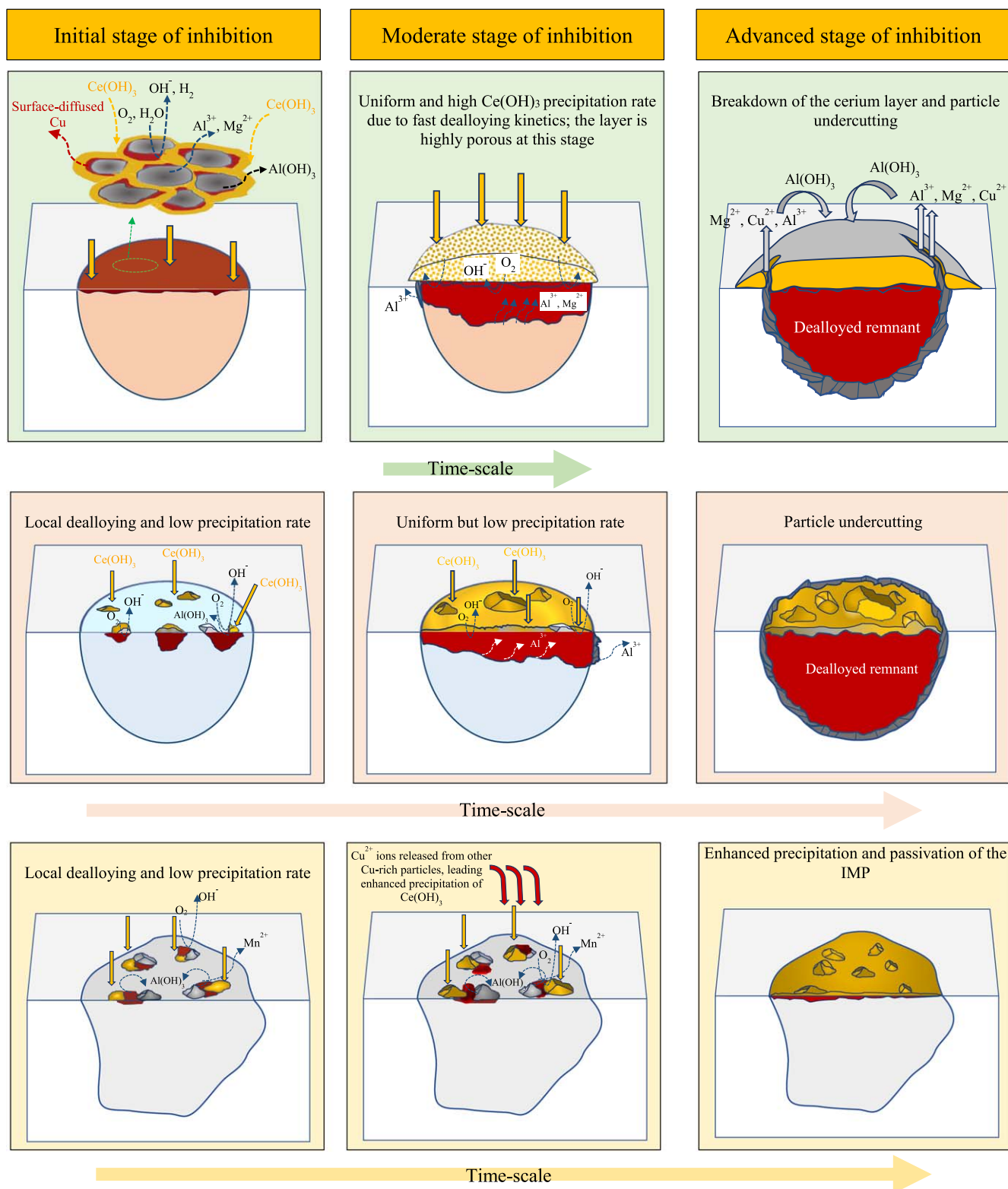
Figure 16. Dealloying-driven cerium deposition on IMPs in AAs. 3D schematic view of the mechanism of cerium precipitation mechanisms on individual S-phase (boxed in green; upper row), θ-phase (boxed in pink; middle row) and $Al_7Cu_2Fe(Mn)$ constituent phase (boxed in yellow; lower row) embedded in the alloy matrix. The mechanisms by which the cerium precipitates on IMPs along with the probable corrosion reactions occurring at IMPs are depicted in detail.

precipitation compared to that for S-phase particles. Besides, the corrosion of Al_2Cu particles in cerium-containing solution ends up with an undercut dealloyed remnant which is covered with a thin mixed layer of cerium and aluminium (hydr)oxides. Constituent phases are very stable in the solution and slightly endure dealloying

over long-term exposure. $Al_7Cu_2Fe(Mn)$ particles are found either discretely or fully covered with a thin cerium-based layer at prolonged exposure times. The latter is caused by the redeposited copper nanoparticles that accelerate the dealloying rate, effectively enhancing the cerium precipitation. $Al_{76}Cu_6Fe_7Mn_5Si_6$ particles, if

slightly dealloyed, do not interact with cerium. The cerium deposit can be a mixture of Ce(IV) and Ce(III) oxides as the valence transformation happens with prolonged exposure time. This phenomenon was linked to an oxidising reaction either due to the presence of H_2O_2 or happing on Cu-rich regions of the corroding IMPs. The early electrochemical response (i.e., the first 24 h) of the systems is attributed merely to the morphological and compositional evolutions of S-phase particles, leading to the elevated OCP and LPR values. After 24 h, AA2024-T3 system experiences a stabilised condition due to sluggish evolutions of Al_2Cu and constituent phase particles after 24 h of exposure.

ORCID

P. Visser https://orcid.org/0000-0002-6388-382X
H. Terryn https://orcid.org/0000-0003-2639-5496
J. M. C. Mol https://orcid.org/0000-0003-1810-5145

References

1. A. E. Hughes, N. Birbilis, J. M. Mol, S. J. Garcia, X. Zhou, and G. E. Thompson, "High Strength Al-Alloys: Microstructure, Corrosion and Principles of Protection." *Recent Trends in Processing and Degradation of Aluminium Alloys*, ed. Z. Ahmad 1, 223 (2011).
2. C. Örnek, C. Leygraf, and J. Pan, *J. Electrochem. Soc.*, **167**, 081502 (2020).
3. A. Boag, A. Hughes, A. Glenn, T. Muster, and D. McCulloch, *Corros. Sci.*, **53**, 17 (2011).
4. N. Birbilis and R. Buchheit, *J. Electrochem. Soc.*, **155**, C117 (2008).
5. N. Birbilis and R. G. Buchheit, *J. Electrochem. Soc.*, **152**, B140 (2005).
6. Y. Zhu, K. Sun, and G. Frankel, *J. Electrochem. Soc.*, **165**, C807 (2018).
7. R. Buchheit, M. Martinez, and L. Montes, *J. Electrochem. Soc.*, **147**, 119 (2000).
8. G. S. Frankel and R. L. McCreery, *Interface-Electrochemical Society*, **10**, 34 (2001).
9. M. Kendig and R. Buchheit, *Corrosion*, **59**, 379 (2003).
10. G. Ilevbare, J. Scully, J. Yuan, and R. Kelly, *Corrosion*, **56**, 227 (2000).
11. O. Gharbi, S. Thomas, C. Smith, and N. Birbilis, *npj Materials Degradation*, **2**, 1 (2018).
12. N. Birbilis, R. G. Buchheit, D. Ho, and M. Forsyth, *Electrochemical and Solid State Letters*, **8**, C180 (2005).
13. D. Ho, N. Brack, J. Scully, T. Markley, M. Forsyth, and B. Hinton, *J. Electrochem. Soc.*, **153**, B392 (2006).
14. A. Uhart, J. B. Ledeuil, D. Gonbeau, J.-C. Dupin, J.-P. Bonino, F. Ansart, and J. Esteban, *Appl. Surf. Sci.*, **390**, 751 (2016).
15. M. Mouanga, F. Andreatta, M.-E. Druart, E. Marin, L. Fedrizzi, and M.-G. Olivier, *Corros. Sci.*, **90**, 491 (2015).
16. L. Kasten, J. Grant, N. Grebasch, N. Voevodin, F. Arnold, and M. Donley, *Surf. Coat. Technol.*, **140**, 11 (2001).
17. D. Arnott, N. Ryan, B. Hinton, B. Sexton, and A. Hughes, *Appl. Surf. Sci.*, **22**, 236 (1985).
18. T. Hu, H. Shi, T. Wei, F. Liu, S. Fan, and E.-H. Han, *Corros. Sci.*, **95**, 152 (2015).
19. T. Matsuda, K. B. Kashi, K. Fushimi, and V. J. Gelling, *Corros. Sci.*, **148**, 188 (2019).
20. A. Hughes, T. Markley, S. Garcia, and J. Mol, *Corrosion Engineering, Science and Technology*, **49**, 674 (2014).
21. A. Mishra and R. Balasubramaniam, *Corrosion*, **63**, 240 (2007).
22. P. Rodič and I. Milošev, *J. Electrochem. Soc.*, **163**, C85 (2015).
23. H. Shi, E.-H. Han, and F. Liu, *Corros. Sci.*, **53**, 2374 (2011).
24. S. Garcia, T. Markley, J. Mol, and A. Hughes, *Corros. Sci.*, **69**, 346 (2013).
25. S. A. Hayes, P. Yu, T. J. O'Keefe, M. J. O'Keefe, and J. O. Stoffer, *J. Electrochem. Soc.*, **149**, C623 (2002).
26. K. A. Yasakau, M. L. Zheludkevich, S. V. Lamaka, and M. G. Ferreira, *J. Phys. Chem. B*, **110**, 5515 (2006).
27. L. Paussa, F. Andreatta, D. De Felicis, E. Bemporad, and L. Fedrizzi, *Corros. Sci.*, **78**, 215 (2014).
28. J. Li, B. Hurley, and R. Buchheit, *J. Electrochem. Soc.*, **163**, C845 (2016).
29. A. J. Aldykewicz, H. S. Isaacs, and A. J. Davenport, *J. Electrochem. Soc.*, **142**, 3342 (1995).
30. P. Campestrini, H. Terryn, A. Hovestad, and J. H. W. de Wit, *Surf. Coat. Technol.*, **176**, 365 (2004).
31. M. L. Zheludkevich, R. Serra, M. F. Montemor, K. A. Yasakau, I. M. M. Salvado, and M. G. S. Ferreira, *Electrochim. Acta*, **51**, 208 (2005).
32. N. C. Rosero-Navarro, M. Curioni, R. Bingham, A. Durán, M. Aparicio, R. A. Cottis, and G. E. Thompson, *Corros. Sci.*, **52**, 3356 (2010).
33. A. Kosari, H. Zandbergen, F. Tichelaar, P. Visser, P. Taheri, H. Terryn, and J. M. C. Mol, *Corros. Sci.*, **177**, 108912 (2020).
34. A. Kosari, F. Tichelaar, P. Visser, H. Zandbergen, H. Terryn, and J. M. C. Mol, *Corros. Sci.*, **177**, 108947 (2020).
35. L. A. J. Garvie and P. R. Buseck, *J. Phys. Chem. Solids*, **60**, 1943 (1999).
36. V. J. Keast, A. J. Scott, R. Brydson, D. B. Williams, and J. Bruley, *J. Microsc.*, **203**, 135 (2001).
37. A. Davenport, H. Isaacs, and M. Kendig, *Corros. Sci.*, **32**, 653 (1991).
38. U. Tiringer, A. Durán, Y. Castro, and I. Milošev, *J. Electrochem. Soc.*, **165**, C213 (2018).
39. T. K. Shruthi and G. M. Swain, *J. Electrochem. Soc.*, **166**, C3284 (2019).
40. A. Hughes, A. Boag, A. Glenn, D. McCulloch, T. Muster, C. Ryan, C. Luo, X. Zhou, and G. Thompson, *Corros. Sci.*, **53**, 27 (2011).
41. N. Birbilis, T. H. Muster, and R. G. Buchheit, *Corrosion Mechanisms in Theory and Practice*, ed. P. Marcus (CRC Press, London) 3, 705 (2011).
42. T. Sata and M. Yoshimura, *J. Ceram. Assoc. Japan*, **76**, 116 (1968).